Title	Attraction of neutrally buoyant deformable particles towards a vortex
Author(s)	Fujiki, Yutaro; Awai, Hideto; Motoori, Yutaro et al.
Citation	Physical Review Fluids. 2024, 9(1), p. 014301
Version Type	VoR
URL	https://hdl.handle.net/11094/100038
rights	Copyright 2024 by the American Physical Society
Note	

PHYSICAL REVIEW FLUIDS **9**, 014301 (2024)

Attraction of neutrally buoyant deformable particles towards a vortex

Yutaro Fujiki, Hideto Awai, Yutaro Motoori, and Susumu Goto
Graduate School of Engineering Science, Osaka University, 1-3 Machikaneyama, Toyonaka, Osaka, 560-8531 Japan

(Received 6 March 2023; accepted 30 November 2023; published 4 January 2024)

We conduct direct numerical simulations (DNS) by the full Eulerian finite difference method of a neutrally buoyant hyperelastic particle in Taylor–Green vortical flow. We investigate the case that the initial shape of the particle is spherical with a diameter comparable with the vortex radius. The particle orbit depends on the degree of its deformation due to the flow. When the particle is stiffer (i.e., the capillary number Ca is smaller than about 0.1), the particle is hardly deformed and slowly swept out from the vortex. In contrast, softer particles with Ca $\gtrsim 0.1$ are significantly deformed, in an initial period, and they are attracted towards the vortex; then, afterward, the deformation is relaxed so that they can stay around the vortex center. Such an attraction of anisotropic neutrally buoyant particles towards a vortex occurs, even if particles are rigid. We demonstrate this phenomenon by additional DNS of a rigid prolate spheroidal particle in the vortical flow. We also develop analytical arguments to show that the angle between the major axis of the particle and the pathline determines whether the vortex attracts or repulses the particle. This feature well explains the radial motion of neutrally buoyant elastic particles in vortical flow.

DOI: 10.1103/PhysRevFluids.9.014301

I. INTRODUCTION

Fluid-particle interaction is one of the most fundamental issues in fluid mechanics and it plays a crucial role in many circumstances. Among various phenomena caused by fluid-particle interactions, in the present study we treat a fundamental problem; namely, particle orbits about a tubular vortex. For example, bubbles in water swirl around a vortex tube and finally accumulate into the vortex core. This phenomenon is well known and we sometimes utilize it for flow visualizations. On the other hand, heavy particles are centrifuged out from vortices. These phenomena occur when the velocity relaxation time τ_p of particles is sufficiently longer than the characteristic timescale of vortices, i.e., ω^{-1} with ω being the vorticity. This is because if $\tau_p \ll \omega^{-1}$, then particles can follow swirling flow and behave like a tracer. Here, under the assumption that the particle is spherical and the fluid force is approximated by the Stokes drag, we may estimate the velocity relaxation time as

$$\tau_p = \frac{\rho^{(p)} D^2}{18\rho^{(f)}\nu^{(f)}}, \tag{1}$$

where D and $\rho^{(p)}$ are the diameter and mass density of the particle, respectively; and $\rho^{(f)}$ and $\nu^{(f)}$ are the mass density and kinematic viscosity of the fluid. Hence, in general, particle's attraction and repulsion by vortices occur when the particle size D or the density ratio $\rho^{(p)}/\rho^{(f)}$ is large enough.

We can easily treat particles with small D, because if the particle Reynolds number is low enough, then fluid-particle interaction is simple. In fact, there are many previous studies on the clustering of pointwise particles in vortical flow. This phenomenon, that is the clustering of small particles, is sometimes called the preferential concentration [1], which occurs, as mentioned above, for particles with mass density different from fluid density. The clustering is observed even in statistically homogeneous turbulent flows [1–8] because turbulence is composed of a hierarchy of coherent vortices [9–12]. This is also the case in wall turbulence, and many authors explained the clustering phenomena in terms of coherent flow structures [13–20]. Particle clustering plays an important role in many phenomena including the planet formation [21], droplet growth in cloud [22], cell culture in bioreactors [23], and so on because it enhances the collision of particles. Apart from clustering, the vortex action on small particles is also important in some fundamental problems such as the effects on the settling velocity of particles in turbulence [24] or the effect of the secondary flow (the Dean vortex) in a curved tube on the Segre–Silberberg effect [25,26].

We may explain the clustering of small particles with long enough τ_p in vortical flow. When the particle Reynolds number is small, particles move by the Stokes drag and added mass force. Suppose that flow $\boldsymbol{u}$ is turbulence, which is composed of vortices with a range of turnover times. Then, since particles cannot follow fluid motion faster than τ_p, their motions are approximated by those in the coarse-grained flow $\boldsymbol{u}_>$ where flow faster than τ_p is removed [7,8]. Then, Maxey's argument [27] leads to the conclusion that the particle velocity *field*, $\boldsymbol{v}_p$, obeys

$$\nabla \cdot \boldsymbol{v}_p = -\tau_p (\beta - 1) Q_> . \tag{2}$$

Here, $Q_>$ is the second invariant of the gradient of $\boldsymbol{u}_>$ and β $(= 3\rho^{(f)}/(2\rho^{(p)} + \rho^{(f)}))$ is the mass parameter which is smaller/lager than 1 when particles are heavier/lighter than the fluid. Since $Q_>$ is positive/negative inside/outside vortices, (2) describes the clustering of small particles. Heavy particles are swept out from vortices, where $Q_> \gg 0$, whereas light ones accumulate into the vortices. In other words, neutrally buoyant small particles ($\beta = 1$) behaves like a tracer, and they do not cluster by the action of vortices.

Thus, the clustering of particles with $\beta \neq 1$ is well understood for small, i.e., point-wise, particles. It is however unknown whether or not particles can form clusters when they have finite sizes. If particle mass density $\rho^{(p)}$ is different from fluid density $\rho^{(f)}$, then the aforementioned preferential concentration for small particles can occur even for finite-size ones. Therefore, the target of the present study is neutrally buoyant finite-size particles.

More concretely, we investigate the fundamental process of the accumulation of *nonspherical* neutrally buoyant particles in vortical flow. The main conclusions will be the following. (i) Even if a particle is neutrally buoyant, if it is finite-size and nonspherical, then it can be attracted or repulsed by vortices. (ii) If the particle is elastic and deformable, then the shear flow around a vortex can deform the particle, and it is attracted to the vortex. Then, once the particle migrates into the vortex core, its deformation is relaxed so that it can stay there.

Since conclusion (ii) is related to deformable particles, it is worth presenting relevant studies of deformable neutrally buoyant particles in turbulence. For example, Ray and Vincenzi [28] numerically simulated small deformable particles in isotropic turbulence to show the statistics of their deformation and breakup. Hajisharifi *et al.* [29,30] also simulated wall turbulence with finite-size deformable particles, and point-wise ones, to examine particle-turbulence interactions. Although these are pioneering studies, since the behavior of deformable particles in turbulence is complex, there are also studies of such particles in simpler systems. As a particularly relevant study to the present one, Kabacaoğlu and Lushi [31] recently investigated vesicular particles, which contain a fluid inside, in the Taylor–Green vortex flow, and showed that the particle behavior depended on its deformability and the viscosity ratio.

In the rest of the present article, after describing numerical method (Sec. II), we first demonstrate in Sec. III the phenomenon (ii) of the attraction of deformable particles towards a vortex by means of direct numerical simulations (DNS) of elastic particles around the Taylor–Green columnar vortices by full Eulerian finite difference method [32]. Then, conducting additional DNS by immersed boundary method [33,34] of rigid spheroidal particles (Sec. IV A) and developing theoretical arguments in two-dimensional flow (Sec. IV B), we show the physical mechanism of the phenomenon (i), and explain the numerical observation (ii) for elastic particles.

II. NUMERICAL METHODS

A. Governing equations

We investigate the motion of neutrally buoyant incompressible hyperelastic particles in an incompressible Newtonian fluid. Then, the continuity equation and the equations of motion have a common expression both for particles and fluid phases as

$$\frac{\partial v_i^{(\alpha)}}{\partial x_i} = 0 \tag{3}$$

and

$$\rho\left(\frac{\partial v_i^{(\alpha)}}{\partial t} + v_j^{(\alpha)}\frac{\partial v_i^{(\alpha)}}{\partial x_j}\right) = \frac{\partial \sigma_{ij}^{(\alpha)}}{\partial x_j}, \tag{4}$$

respectively. Here, $\rho\ (= \rho^{(f)} = \rho^{(p)})$ is the mass density, and $v_i^{(\alpha)}(\boldsymbol{x}, t)$ and $\sigma_{ij}^{(\alpha)}(\boldsymbol{x}, t)$ are the velocity and stress tensor at position $\boldsymbol{x}$ and time t. Superscript α is either p for particles or f for fluid. We assume a Newtonian fluid for the fluid phase and a hyperelastic particle with the Saint Venant–Kirchhoff model [35,36]. Then the stress tensor $\sigma_{ij}^{(\alpha)}$ in Eq. (4) is expressed as

$$\sigma_{ij}^{(f)} = \mu^{(f)}\left(\frac{\partial v_i^{(f)}}{\partial x_j} + \frac{\partial v_j^{(f)}}{\partial x_i}\right) \tag{5}$$

for the fluid and

$$\sigma_{ij}^{(p)} = \mu^{(p)}\left(\frac{\partial v_i^{(p)}}{\partial x_j} + \frac{\partial v_j^{(p)}}{\partial x_i}\right) + \mu_{\mathrm{lame}}(B_{ik}B_{kj} - B_{ij}) + \frac{1}{2}\,\lambda_{\mathrm{lame}}(\mathrm{tr}(B_{ij}) - 3)B_{ij} \tag{6}$$

for the particles. Here, $\mu^{(\alpha)}$ is the viscosity and μ_{lame} and λ_{lame} are Lamé's constants of the particles. In Eq. (6), B_{ij} is the left Cauchy–Green tensor, which obeys

$$\frac{\partial B_{ij}}{\partial t} + v_k\frac{\partial B_{ij}}{\partial x_k} - \frac{\partial v_i}{\partial x_k}B_{kj} - B_{ik}\left(\frac{\partial v_k}{\partial x_j}\right)^T = 0. \tag{7}$$

We impose the triply periodic boundary conditions for the cubic domain with side 2π. The boundary conditions between the particle and fluid phases are the continuity conditions of the velocity, $v_i^{(f)} = v_i^{(p)}$, and the stress, $\sigma_{ij}^{(f)}n_j = \sigma_{ij}^{(p)}n_j$, with n_i being the unit normal vector on the boundary.

B. Numerical scheme

We use a full Eulerian finite difference method [32], where the governing equations both for the fluid and particle phases are solved in the Eulerian coordinate. In this method, using the volume fraction $\phi(\boldsymbol{x}, t)$, where $\phi = 0$ for the fluid and 1 for the particles, we employ the volume-averaging procedure [37] so that the continuity conditions of the velocity and stress can be automatically satisfied. More concretely, introducing the unified velocity,

$$v_i = (1 - \phi)v_i^{(f)} + \phi v_i^{(p)}, \tag{8}$$

and the unified stress tensor,

$$\sigma_{ij} = (1 - \phi)\sigma_{ij}^{(f)} + \phi\sigma_{ij}^{(p)}, \tag{9}$$

we rewrite Eqs. (3) and (4) as

$$\frac{\partial v_i}{\partial x_i} = 0 \tag{10}$$

and

$$\rho\left(\frac{\partial v_i}{\partial t}+v_j\frac{\partial v_i}{\partial x_j}\right)=\frac{\partial \sigma_{ij}}{\partial x_j}, \tag{11}$$

respectively. Then, we numerically solve Eqs. (10) and (11) together with the advection equation for ϕ,

$$\frac{\partial \phi}{\partial t}+v_j\frac{\partial \phi}{\partial x_j}=0, \tag{12}$$

and Eq. (7). We use the finite difference method on the staggered grid [38]. We estimate the spatial derivatives by the second-order central difference except for the advection terms in Eqs. (7) and (12), for which we use the fifth-order WENO method.

The concrete numerical procedures are as follows. (i) First, we integrate Eqs. (7) and (12) for B_{ij} and ϕ by the second-order Adams–Bashforth scheme. We use the CLSVOF method [39] to avoid the numerical diffusion of ϕ. (ii) Next, we integrate Eq. (11) to obtain v_i, where we use the second-order Adams–Bashforth method for the advection and elastic stress terms, the second-order Crank–Nicolson method for the viscous stress term, and the first-order Euler method for the pressure term. To effectively solve the elliptic partial differential equation for the implicit scheme with space-dependent viscosity, we use the method proposed in Ref. [40], where we use the fast Fourier transform. (iii) Then, by the SMAC method, we solve the Poisson equation to correct v_i and p so that Eq. (10) is satisfied.

C. Numerical setup

An aim of the present study is to show the accumulation of elastic particles into vortices. To this end, we investigate particle motions in the Taylor–Green columnar vortices,

$$\boldsymbol{v}^{(f)}=\frac{\rho f_0(-\sin x\cos y,\cos x\sin y,0)}{2\mu^{(f)}}, \tag{13}$$

which are sustained by the external force,

$$\boldsymbol{f}=f_0(-\sin x\cos y,\cos x\sin y,0), \tag{14}$$

when the Reynolds number $\mathrm{Re}=\rho U\mathcal{L}/\mu^{(f)}$ is sufficiently low. Here, $\mathcal{L}\ (=\pi)$ and $U=\rho f_0/2\mu^{(f)}$ are the size and the maximum swirling velocity of the Taylor–Green vortices. Here, we set $f_0=1$. This flow (13) is simple but useful to investigate the behavior of particles around a vortex. Indeed, Jayaram *et al.* [41] and Kabacaoğlu and Lushi [31] also used the Taylor–Green vortex flow to investigate interactions between particles and a vortex.

Since the Taylor–Green flow (13) is composed of four vortex columns in a periodic cube, we simultaneously track four particles in a single DNS, each of which is located around one of the four vortices. Then, we can investigate the dependence on the internal distance $r(0)$ from the vortex center, we examine four cases $[r(0)=i\mathcal{L}/16$ with $i=3, 4, 5$, and 6] in a single DNS. Note that we set the initial z coordinate of the particles different so that interaction between the particles can be negligible. The initial shape of the particles is spherical with diameter D.

An important dimensionless parameter for particle deformation is the capillary number,

$$\mathrm{Ca}=\frac{\mu^{(f)}U}{\mu_{\mathrm{lame}}D}. \tag{15}$$

In addition to Ca, there are four other dimensionless parameters, which control particle motions: namely, the particle Reynolds number ($\mathrm{Re}_p=\rho UD/\mu^{(f)}$), the dimensionless particle diameter ($\widetilde{D}=D/\mathcal{L}$), the viscosity ratio ($\xi=\mu^{(p)}/\mu^{(f)}$), and the number of particles (N). Fixing $\mathrm{Re}_p=0.01$, $\widetilde{D}=0.375$, $\xi=1$, and $N=4$, we conduct DNS by changing Ca in a wide range from a nearly rigid case ($\mathrm{Ca}=0.01$) to very deformable one ($\mathrm{Ca}=10$). Incidentally, since $\mathrm{Re}_p=0.01$ and $\widetilde{D}=0.375$, the global Reynolds number $\mathrm{Re}=\mathrm{Re}_p/\widetilde{D}\approx 0.027$ is sufficiently small so that the Taylor–Green vortices (13) are stable in the single-phase flow.

It is crucial to confirm that the spatial resolution is fine enough for accurate DNS. We use 256^3 grid points so that the initial particle diameter $D\ (= 0.375\mathcal{L})$ contains 48 grid points, which ensures the sufficient resolution [42]. Concerning the temporal resolution, we set the time increment so that it is smaller than $0.1\max\{T_\mathrm{a}, T_\mathrm{e}\}$, where $T_\mathrm{a} = \Delta x/U$ and $T_\mathrm{e} = \Delta x/\sqrt{\mu_\mathrm{lame}/\rho}$ with Δx being the grid width are the timescales of the advection and the spread of elastic waves, respectively.

III. NUMERICAL RESULTS

A. Attraction of elastic particles towards a vortex

To demonstrate that softer particles tend to accumulate into a vortex center, we show in Fig. 1 the temporal evolution of elastic particles with two different values of the capillary number (Ca = 10 and 0.01). This figure shows the particle position and deformation around one of the four Taylor–Green vortices, the axis of which is denoted by the black straight line, at time $t' = 0$, 2, 4, and 6. Here, $t' = t/\tau_v$ is the time normalized by the swirling time, $\tau_v = 2\pi\mathcal{L}/U$, of the Taylor–Green vortices. We visualize the particle shape by the isosurface of $\phi = 0.5$.

Figure 1(a) (Supplemental movie is also available online [43]) shows that the softer particle with Ca = 10 deforms into a lunar shape for $0 \lesssim t' \lesssim 2$, and it swirls and approaches the vortex center. After reaching the vortex center the particle deformation is relaxed and it becomes cylindrical, and then it stays around there. In contrast, Fig. 1(b) shows that the harder particle (Ca = 0.01) keeps the initial spherical shape and it is slowly swept out from the vortex. These visualizations demonstrate that even if a particle is neutrally buoyant, it can accumulate into a vortex by the effect of the deformation, and that the behavior is dependent on the deformability of the particle.

To quantitatively show the attraction of the deformable particle towards a vortex, we show in Fig. 2(a) the distance $r(t)$ between the particle's mass center $\boldsymbol{x}_G$ and the vortex axis. This figure shows the results with a common initial condition $[r(0) = 5\mathcal{L}/16]$ with four different values of Ca as 10, 1, 0.1, and 0.01. Darker lines correspond to larger Ca. It is evident that a softer particle is attracted towards the vortex center more rapidly; for the softest particle (Ca = 10) only five revolutions results in the attraction to the vortex center. For this initial condition, $r(0) = 5\mathcal{L}/16$, the hardest particle with Ca = 0.01 is swept out from the vortex (as observed in Fig. 1). Kabacaoğlu and Lushi [31] also observed a similar Ca-dependence of the migration of vesicle particles whose viscosity ratio between inner and outer fluids was about unity. Incidentally, the fast temporal oscillation observed in Fig. 2(a) is due to the nonaxisymmetric property of the Taylor–Green vortex (13).

As observed in Figs. 1 and 2(a), soft particles are rapidly attracted to the vortex center. Therefore, here we investigate particle motion in an initial period (i.e., $t' \lesssim 2$). Figure 2(b) shows the value of the distance $r(t' = 2)$ between the particle and vortex axis for different values of Ca. The distance $r(t' = 2)$ is a monotonically decreasing function of Ca, and if Ca $\lesssim 0.1$, then the particle is swept out from the vortex, otherwise it accumulates into the vortex.

We have shown only the result with a fixed initial condition $[r(0) = 5\mathcal{L}/16]$, but even for different initial locations, $r(0) = i\mathcal{L}/16$ with $i = 3$, 4, and 6, particles with Ca $\gtrsim 0.1$ are eventually attracted to the vortex. Evidence for Ca = 10 is shown in Fig. 3(a). The degree of deformation shown in Fig. 3(b) will be discussed in the next subsection.

In summary, Ca $\gtrsim 0.1$ is the condition for the attraction of the particle towards the vortex center, and softer particles with larger Ca more rapidly accumulate into the vortex center.

B. Deformation of particles

As observed in the previous subsection, the deformation is essential for the attraction of the particles towards the vortex center. We estimate the inertial tensor G_{ij} of a particle by

$$G_{ij} = \frac{\int \phi(x_i - x_{Gi})(x_j - x_{Gj})dV}{\int \phi dV}, \tag{16}$$

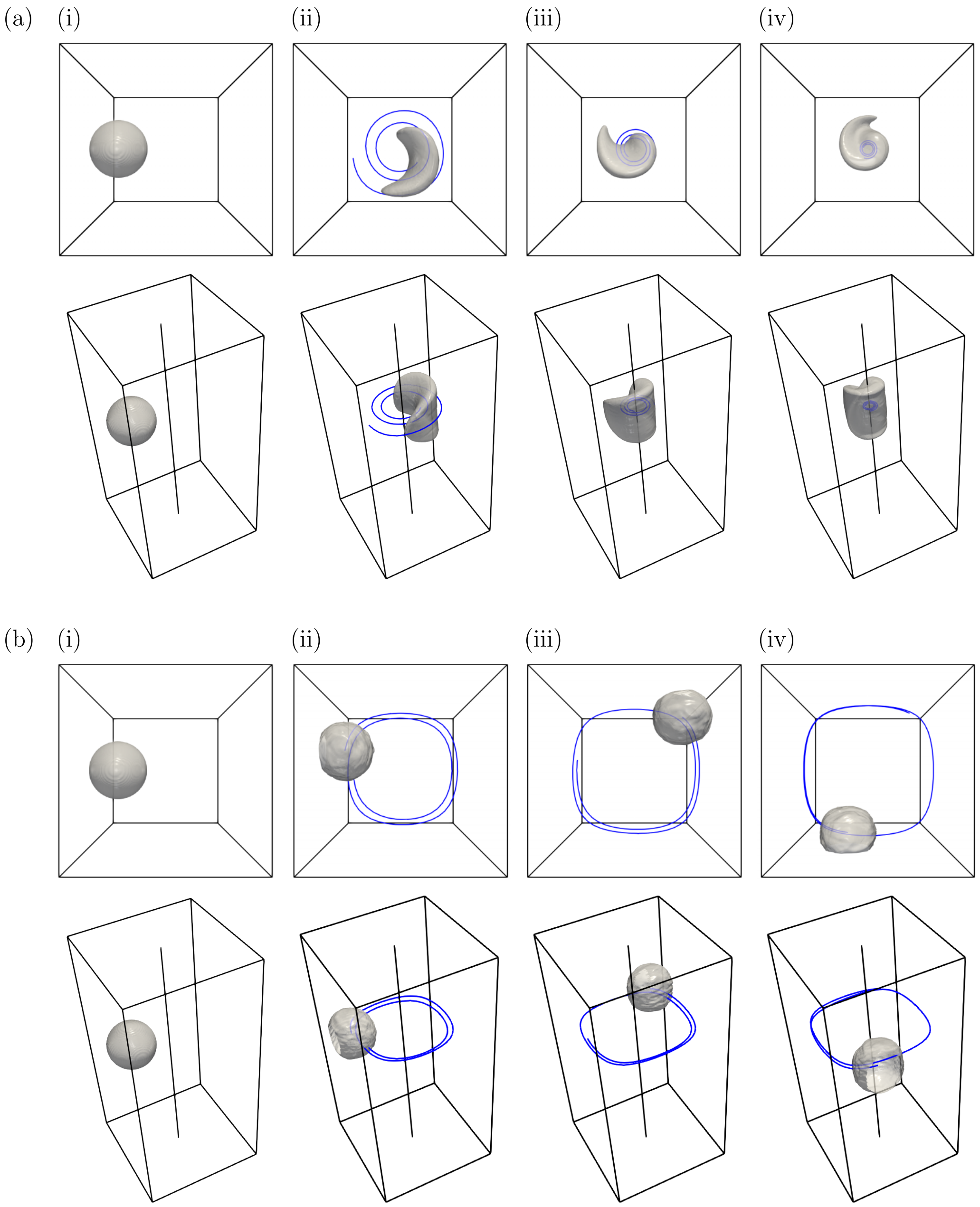

FIG. 1. (a) Location and deformation of an elastic particle with $\mathrm{Ca} = 10$ at (i) $t' = 0$, (ii) 2, (iii) 4, and (iv) 6. The blue curve denotes the orbit during (ii) $0 \leqslant t' \leqslant 2$, (iii) $2 \leqslant t' \leqslant 4$, and (iv) $4 \leqslant t' \leqslant 6$. The solid black line is the axis of the Taylor–Green vortex. (b) Similar to panel (a) but for a particle with $\mathrm{Ca} = 0.01$. Supplemental movie for panel (a) is available online [43].

where $\boldsymbol{x}_G$ is the center of mass of the particle. We have confirmed that one of the principal axis of G_{ij} is almost perfectly parallel to the z axis; more precisely, even in the most deformable case with $\mathrm{Ca} = 10$, the cosine of the angle between the principal axis and the z axis is 0.999, which is the average over four initial conditions and over the time between $0 \leqslant t' \leqslant 10$. Therefore, we use the

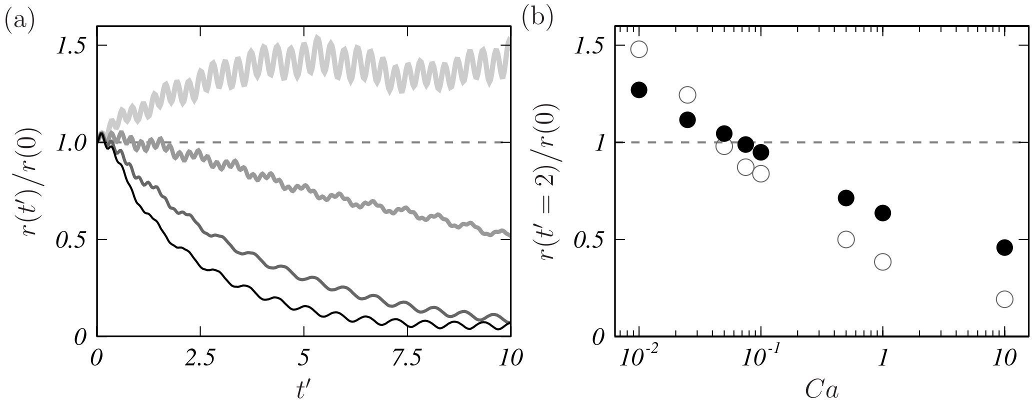

FIG. 2. (a) Temporal evolution of the distance $r(t)$ between the elastic particle's mass center and the axis of the Taylor–Green vortex. The initial condition is $r(0) = 5\mathcal{L}/16$. Different lines correspond to results with different values of the capillary number: Ca = 10, 1, 0.1, and 0.01 from dark to light colors. (b) The Ca-dependence of the distance $r(t')$ at time $t' = 2$ (●) and $t' = 4$ (○).

two eigenvalues λ_1 and λ_2 ($\lambda_1 > \lambda_2$) corresponding to the principal axes on the x-y plane to quantify the deformation on the plane by the Taylor parameter,

$$T = \frac{\lambda_1 - \lambda_2}{\lambda_1 + \lambda_2}. \tag{17}$$

This parameter takes a value in the range $0 \leqslant T \leqslant 1$, and $T = 0$ and 1 correspond to a circle and a line, respectively.

We show the temporal evolution of T for the four different values of Ca in Fig. 4(a), where we observe that the deformation in the initial period ($t' \lesssim 5$) is more pronounced for softer particles (i.e., larger Ca). Looking at the softest case (i.e., Ca = 10), we notice that the deformation is initially large (T attains its maximum at $t' \approx 0.43$) and then the deformation gradually becomes smaller for $t' \gtrsim 5$. It is important that $t' \approx 5$ is the time when the particle reached at the center of the vortex [see Fig. 2(a)]. This implies that the soft particle is significantly deformed in the initial period to

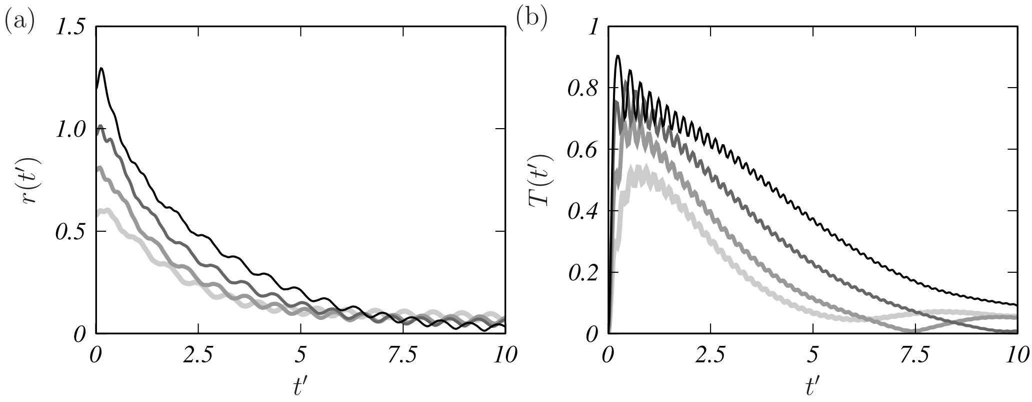

FIG. 3. Initial-condition dependence of the location and deformation of the elastic particle with Ca = 10. We show (a) the distance $r(t')$ from the vortex axis and (b) Taylor parameter $T(t')$, which is defined by Eq. (17), as functions of the normalized time t'. Four different curves denote results with different initial locations: $r(0) = i\mathcal{L}/16$ with $i = 3$, 4, 5 and 6 from lighter (thicker) to darker (thinner) lines.

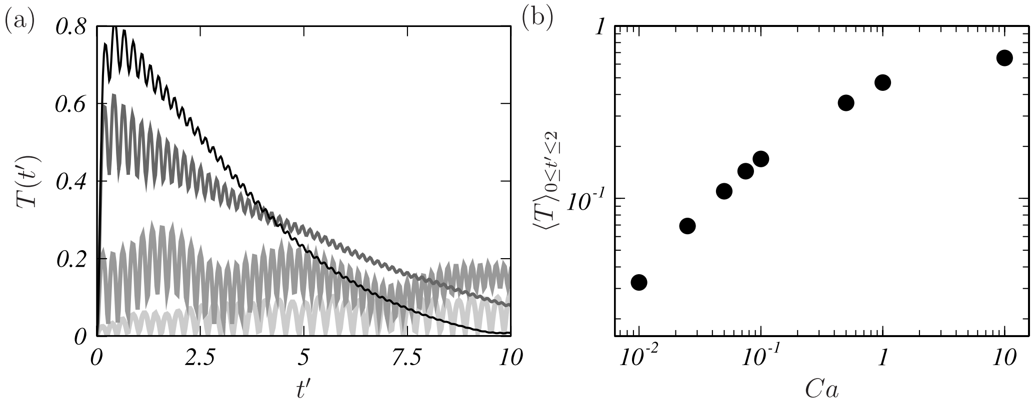

FIG. 4. (a) Temporal evolution of the Taylor parameter $T(t)$ defined by Eq. (17). Similarly to Fig. 2(a), different lines correspond to different Ca. (b) The Ca-dependence of the temporal average $\langle T\rangle_{0\leqslant t'\leqslant 2}$ of T in the period $0 \leqslant t' \leqslant 2$. The initial condition is $r(0) = 5\mathcal{L}/16$.

be attracted towards the center of the vortex, and then the deformation becomes weaker so that the particle can stay inside the vortex. This is consistent with the observation in Fig. 1(a); that is, the particle deforms into the lunar shape during the attraction towards the center of the vortex ($t' \lesssim 5$), while it stays in the vortex with a cylindrical shape ($t' \gtrsim 5$). Note that $T \to 0$ in the final period corresponds to a cylindrical, rather than spherical, shape of the particle [see Fig. 1(a)–1(iv)]. Incidentally, similar temporal evolution of the deformation is observed irrespective of the initial location, $r(0)$, of the particle with Ca = 10 [Fig. 3(b)].

We show the Ca-dependence of the temporal average $\langle T\rangle_{0\leqslant t'\leqslant 2}$ in the period $0 \leqslant t' \leqslant 2$ in Fig. 4(b). It is of importance that $\langle T\rangle_{0\leqslant t'\leqslant 2}$ is a monotonically increasing function of Ca. This result implies that Ca determines the initial deformation of the particles, and more deformed particles can be more rapidly attracted to the center of the vortex.

IV. DISCUSSIONS

A. Importance of the incline angle

The observations in Figs. 2 and 4 imply the correlation between the degree T of the deformation and the attraction towards the vortex center. However, in this section, we emphasize that the deformation of a particle is a necessary condition for the attraction. Another important factor is the angle between the anisotropic particle and the pathline of the fluid particle.

To demonstrate the importance of the orientation of the anisotropic particle with respect to pathline, we show here numerical results of the motion of a rigid prolate spheroidal particle. To this end, we conduct another simulation for rigid spheroidal particles in the Taylor–Green vortical flow by the immersed boundary method [34]. The fluid parameters are same as for the DNS of elastic particles. Details of the numerical methods are given in the Appendix.

First, let us observe in Fig. 5 the temporal evolution of a prolate spheroidal particle with the Taylor parameter $T = 0.5$ and the volume same as the examined elastic particles. The angle of the particle is initially set as in Fig. 5(a) so that its major axis is parallel to the pathline, which is the streamline in steady flow, of the Taylor–Green vortex. The particle swirls about the vortex, but it is important to see that the distance from the center of the vortex is not monotonic. Looking at the particle orbit in the period $0 \leqslant t' \leqslant 1.5$ in Figs. 5(a) and 5(b), we can see that the particle is swept out from the vortex. However, the orbit in Fig. 5(c) shows that the particle is attracted to the vortex in the period $1.5 \leqslant t' \leqslant 3$.

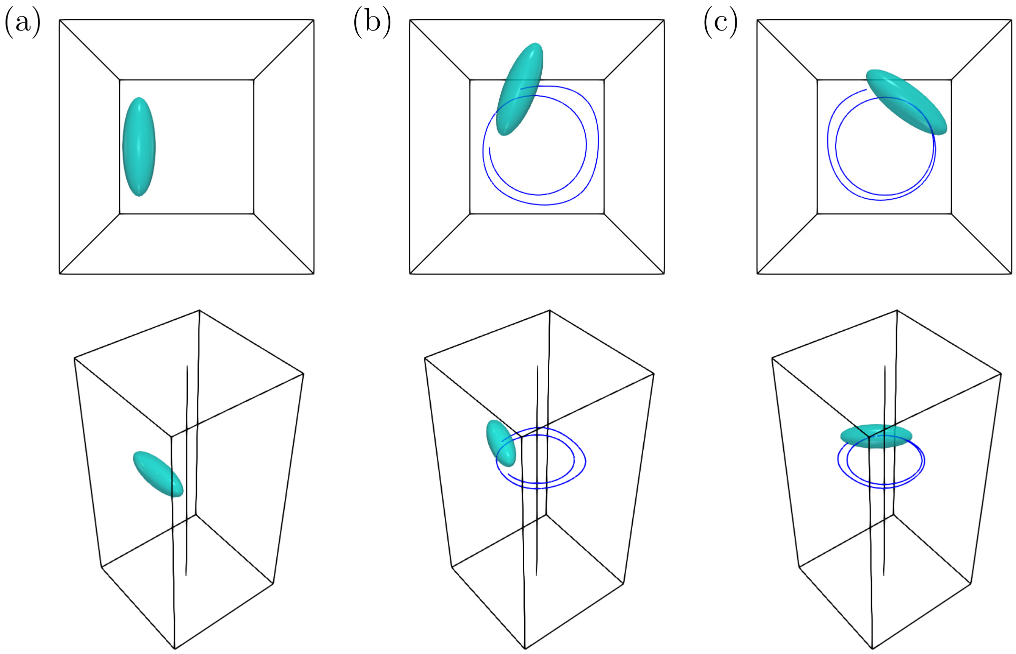

FIG. 5. Location and orientation of the rigid prolate spheroidal particle with $T = 0.5$ at (a) $t' = 0$, (b) 1.5, and (c) 3. The black line is the vortex axis, and the blue line is the trajectory of the particle in the periods (b) $0 \leqslant t' \leqslant 1.5$ and (c) $1.5 \leqslant t' \leqslant 3$.

We can confirm this nonmonotonic behavior also in Fig. 6(a), where the black thin line shows the distance r between the particle and vortex. We also plot in Fig. 6(a) results for rigid spheroidal particles with $T = 0.3$ (gray) and 0.2 (light gray). Stronger anisotropy (i.e., larger T) leads to the larger nonmonotonic radial motion of the particle. Besides, we can observe a similar periodic behavior for the particle initially placed with its major axis perpendicular to the pathline, although in

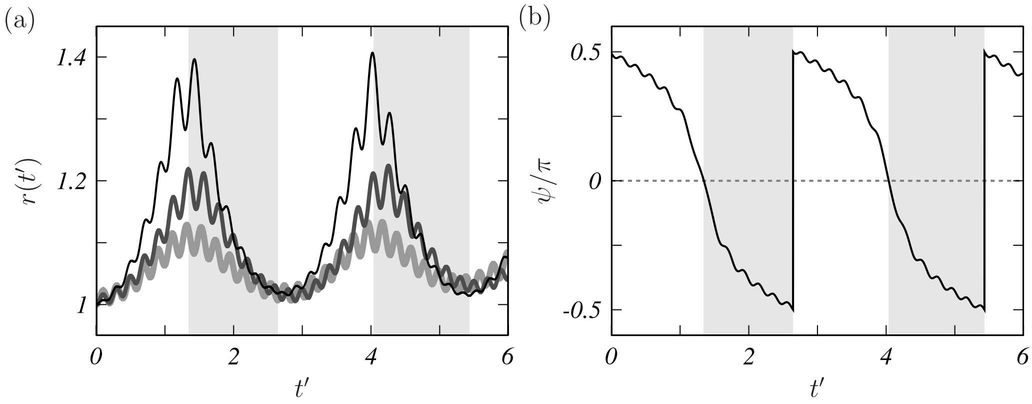

FIG. 6. (a) Temporal evolution of the distance r between the vortex axis and the particle center. The light gray, gray and black lines show the results for $T = 0.2$, 0.33, and 0.5, respectively. (b) Temporal evolution of the angle ψ [see Fig. 7(a)] for $T = 0.5$. The dashed line indicates $\psi = 0$. Shaded periods in both panels correspond to the internals with $\psi < 0$ for $T = 0.5$.

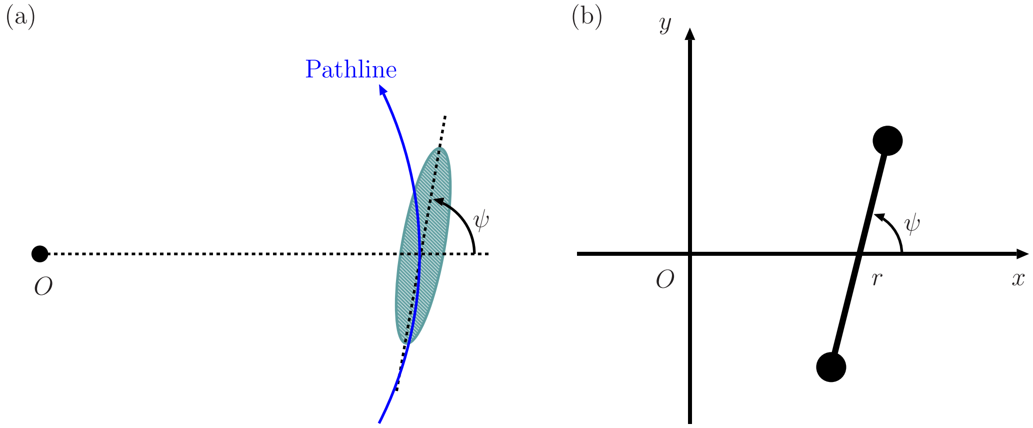

FIG. 7. The definition of ψ, which is the angle between the major axis of the prolate spheroidal particle and the radial direction. Here, O denotes the center of the vortex. (b) The rod model examined in Sec. IV B, which is composed of two neurally buoyant particles connected by a massless rod with length L. The angle ψ is defined similarly to panel (a).

such a case it initially moves inward instead of outward (figure is omitted). However, we emphasize that the anisotropic shape is not sufficient to explain the accumulation of the elastic particles into the vortex center.

To show the importance of the orientation of the particle with respect to the pathline, we define angle ψ as in Fig. 7(a); ψ is the angle between the major radius of the spheroidal particle and the radial direction. Hence, the angle between the major radius and the pathline is $\psi - \pi/2$, if the vortex is axisymmetric. We set the range of ψ as $-\pi/2 \leqslant \psi \leqslant \pi/2$. Note that $\psi = \pi/2$ and $-\pi/2$ correspond to the same orientation. When $\psi < 0$ (or $\psi > 0$), the major radius is inwardly (or outwardly) inclined with respect to the path line.

We show in Fig. 6(b) the temporal evolution of ψ for the spheroidal particle with $T = 0.5$ (shown in Fig. 5). The shaded periods in Fig. 6 correspond to those with $\psi < 0$. Looking again at the black thin line in Fig. 6(a), it is evident that when $\psi < 0$ the particle accumulates into the center of the vortex (i.e., $dr/dt < 0$), whereas it is swept out from the vortex (i.e., $dr/dt > 0$) when $\psi > 0$.

In fact, it is the angle ψ that also controls the attraction of the elastic particles (Fig. 1) towards the vortex. To show this, we define ψ for the deformed particle by using the eigen-vector of G_{ij} corresponding to λ_1 in place of the major axis of the spheroid. Then, we plot in Fig. 8(a) the temporal evolution of ψ for four different values of Ca. The angle ψ is mostly negative. More precisely, $\psi < 0$ in the initial period ($t' \lesssim 5$) when the particle with Ca $\gtrsim 1$ is significantly deformed. We emphasize that this is similar to the observation in Fig. 6(b) that the rigid spheroidal particle migrates into the vortex center when $\psi < 0$. Therefore, we may conclude that both the anisotropy T and the angle ψ are important for the attraction of particles towards a vortex. In fact, analytical arguments in the next subsection imply that the product of T and $\sin\psi$ (rather than ψ) is the key to the explanation of the attraction. To demonstrate this, we show in Fig. 8(b) the temporal average $\langle T \sin\psi \rangle_{0 \leqslant t' \leqslant 2}$ in the initial period $0 \leqslant t' \leqslant 2$. Comparing this panel with Fig. 2(b), we can see that $|\langle T \sin\psi \rangle|$ indeed correlates with the attraction rate of the particle to the vortex. We can also see that for the examined deformable particles, the Taylor parameter T mainly determines the attraction rate, since $\psi < 0$ irrespective of Ca [see Fig. 8(a)]. This explains the reason why the particles with larger Ca are more rapidly attracted to the vortex (Fig. 2).

To summarize results in this subsection, a rigid prolate spheroidal particle moves nonmonotonically in the radial direction of the vortex; more precisely, the particle is periodically attracted and repelled by the vortex [Figs. 5 and 6(a)]. This behavior is related to the orientation of the particle

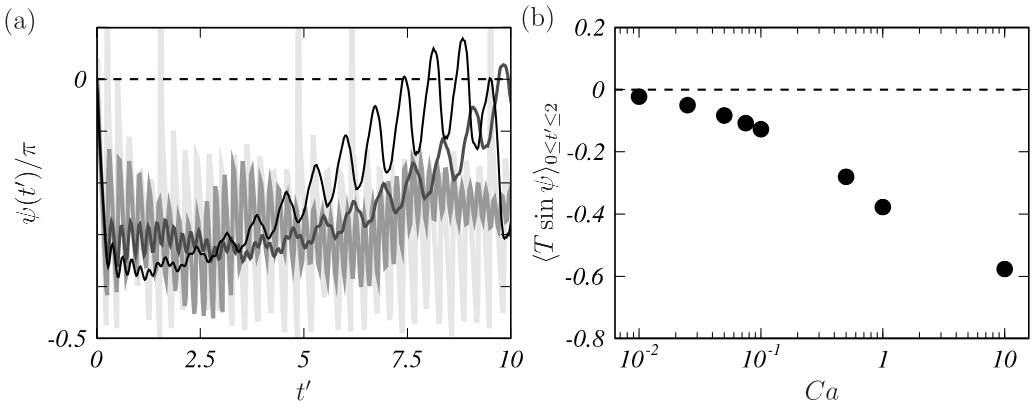

FIG. 8. (a) Temporal evolution of ψ of the elastic particles. Different lines correspond to results with different values of Ca: 10, 1, 0.1 and 0.01 from dark to light colors. (b) The Ca-dependence of the temporal average of $\langle T \sin\psi \rangle$ over the period $0 \leqslant t' \leqslant 2$.

with respect to pathline [Fig. 6(b)]. When the particle head is inclined inwardly with respect to the pathline, it moves towards the vortex axis; otherwise, the particle is swept out from the vortex. We reemphasize that not only the degree T (Fig. 4) of deformation but also the angle ψ are likely to be important for the movement of elastic particles in the radial direction (Fig. 8).

B. A simple model to explain the attraction towards a vortex

1. Governing equations for the rod model

We have shown that the angle between the particle and pathline plays a crucial role to determine the radial motion of a neutrally buoyant particle in vortical flow. In this subsection, we develop a simple model to explain this behavior. Here, we consider motion of two neutrally buoyant particles connected by a massless rod with length L [Fig. 7(b)], which we call the rod model, in two-dimensional vortical flow,

$$\boldsymbol{u}(\boldsymbol{x}) = \boldsymbol{\omega} \times \boldsymbol{x}, \tag{18}$$

where $\boldsymbol{\omega}$ is a vector parallel to the z axis and its magnitude $\omega(|\boldsymbol{x}|)$ is a function of the distance $|\boldsymbol{x}|$ from the origin. We assume that the inertia of the particles is negligible, and therefore their velocity rapidly tends to the fluid velocity at the position of the each particle. We denote the ith ($i = 1, 2$) particle's position and velocity by $\boldsymbol{x}^{(i)} = (x^{(i)}, y^{(i)})$ and $\boldsymbol{u}^{(i)}$, respectively. Then, the latter can be expressed as

$$\boldsymbol{u}^{(i)} = \boldsymbol{u}(\boldsymbol{x}^{(i)}) = (-\omega^{(i)} y^{(i)}, \omega^{(i)} x^{(i)}), \quad \omega^{(i)} = \omega(|\boldsymbol{x}^{(i)}|) \qquad (i = 1, 2). \tag{19}$$

Here, we have set the x-y coordinates as in Fig. 7(b). We also define the distance $r(t)$ between the center of mass of the model and its angle $\psi(t)$, which is similar to the definition in Fig. 7(a).

Let us derive the governing equations for $r(t)$ and $\psi(t)$. Noting that $\boldsymbol{x}^{(i)}(t)$ is expressed as

$$\boldsymbol{x}^{(1)} = (x^{(1)}, y^{(1)}) = \left(r + \frac{L}{2}\cos\psi, \frac{L}{2}\sin\psi \right), \tag{20a}$$

$$\boldsymbol{x}^{(2)} = (x^{(2)}, y^{(2)}) = \left(r - \frac{L}{2}\cos\psi, -\frac{L}{2}\sin\psi \right), \tag{20b}$$

in terms of $r(t)$ and $\psi(t)$, we can show that the x component of the velocity,

$$\boldsymbol{U} = \tfrac{1}{2}\,(\boldsymbol{u}^{(1)} + \boldsymbol{u}^{(2)}), \tag{21}$$

of the center of mass of the model is, from Eqs. (19) and (20), expressed as

$$U_x = \frac{1}{2}(-\omega^{(1)}y^{(1)} - \omega^{(2)}y^{(2)}) = \frac{L(-\omega^{(1)} + \omega^{(2)}) \sin\psi}{4} = -\frac{LW_- \sin\psi}{4}. \tag{22}$$

Similarly, its y component is expressed as

$$U_y = \frac{1}{2}(\omega^{(1)}x^{(1)} + \omega^{(2)}x^{(2)}) = \frac{rW_+}{2} + \frac{LW_- \cos\psi}{4}. \tag{23}$$

Here, we have defined $W_\pm$ as $\omega^{(1)} \pm \omega^{(2)}$.

Next, we consider the rotational motion of the rod model. Let Ω be the angular velocity of the model about its center of mass. Then, since

$$\frac{L\Omega}{2} = \left(\boldsymbol{u}^{(1)} - \frac{\boldsymbol{u}^{(1)} + \boldsymbol{u}^{(2)}}{2}\right) \cdot \begin{pmatrix} -\sin\psi \\ \cos\psi \end{pmatrix}, \tag{24}$$

we obtain, by substituting Eqs. (19) and (20) into above equation,

$$\Omega = \frac{W_+}{2} + \frac{rW_- \cos\psi}{L}. \tag{25}$$

Note that the angular velocity Ω_G of the center of mass about the origin O is

$$\Omega_G = \frac{U_y}{r} = \frac{W_+}{2} + \frac{LW_- \cos\psi}{4r}. \tag{26}$$

Therefore, in the rotating coordinate which is fixed with the center of mass of the model, the angular velocity is

$$\Omega - \Omega_G = \frac{LW_-}{4r}\left(\frac{4r^2}{L^2} - 1\right)\cos\psi. \tag{27}$$

Thus, we obtain, from Eqs. (22) and (27), the governing equations for $r(t)$ and $\psi(t)$ as

$$\frac{dr}{dt} = -\frac{LW_- \sin\psi}{4} \tag{28}$$

and

$$\frac{d\psi}{dt} = \frac{LW_-}{4r}\left(\frac{4r^2}{L^2} - 1\right)\cos\psi, \tag{29}$$

respectively.

Equation (28) for r immediately leads to the conclusion that the sign of ψ determines the direction of the radial motion of the model. This is consistent with results of the rigid prolate spheroidal particle in vortical flow; recall that the sign of ψ almost perfectly coincides with that of dr/dt (Fig. 6). Before discussing the behaviors of rigid spheroidal and elastic particles (see Sec. IV B 3) on the basis of Eqs. (28) and (29), we briefly discuss the solution to these equations for the rod model in the next subsection.

2. *Behavior of the rod model in vortex*

We discuss the motion of the rod model by using Eqs. (28) and (29). These equations imply that W_- is also important for the motion of the rod model. The simplest example is the solid-body rotational flow, where $\omega(|\boldsymbol{x}|)$ is constant. In this case, W_- vanishes, and therefore $dr/dt = 0$ and $d\psi/dt = 0$, which implies that the rod model is frozen in fluid to keep its initial ψ and r. In general, however, W_- is nonzero, and therefore, as will be shown below, the rod model can migrate in the radial direction.

First, we note that

$$\psi = \pm\pi/2 \tag{30}$$

are steady solutions because $|\boldsymbol{x}^{(1)}| = |\boldsymbol{x}^{(2)}|$ and therefore $W_- = 0$ even if $\omega(|\boldsymbol{x}|)$ is not constant. However, these solutions (30) are unstable. To show this, from Eq. (29), we derive

$$\frac{d\delta\psi}{dt} = \mp\frac{LW_-}{4r}\left(\frac{4r^2}{L^2} - 1\right)\delta\psi \quad (\text{for } \psi = \pm\pi/2) \tag{31}$$

for the infinitesimal perturbation $\delta\psi(t)$ around $\psi = \pm\pi/2$. Here, we have assumed that the rod model is apart from the vortex center so that

$$r > \frac{L}{2}. \tag{32}$$

When $W_- < 0$, according to Eq. (29), ψ monotonically decreases and tends to $\psi = -\pi/2$. Since the coefficient of $\delta\psi$ on the right-hand side of Eq. (31) is negative for $\psi = -\pi/2$, it seems stable. However, since $\psi = +\pi/2$ and $-\pi/2$ correspond to the same state, if there is a negative perturbation $\delta\psi < 0$ at $\psi = -\pi/2$, then ψ becomes $\pi/2 + \delta\psi$. Then, since the coefficient of $\delta\psi$ in Eq. (31) is positive around $\psi = \pi/2$, the solution is unstable. This behavior is exactly what we observe in Fig. 5 for the prolate spheroidal particle; namely, the tumbling motion. Similarly, when $W_- > 0$, ψ monotonically increases and tends to $\pi/2$; and when a perturbation makes ψ to be $-\pi/2 + \delta\psi$, the rod model starts again tumbling with $d\psi/dt > 0$.

3. Behavior of anisotropic particles in vortex

We are now ready to explain, by using the above analysis, the behavior of anisotropic particles in Taylor–Green vortical flow. In the following, we assume $W_- < 0$ because this is the case for the Taylor–Green vortices.

First, we show that Eqs. (28) and (29) well explain the behavior of the rigid spheroidal particle shown in Sec. IV A. According to Eq. (29), when Eq. (32) holds, ψ is a monotonically decreasing function of time. This is consistent with the observation in Fig. 6; Eq. (32) holds and $d\psi/dt < 0$. On the other hand, Eq. (28) implies that the sign of ψ determines the sign of dr/dt. The concrete behavior of the model can be described as follows recalling the definition of ψ shown in Fig. 7. We suppose that, at initial time, the major axis of the prolate spheroidal particle is almost parallel to the pathline, but its head is located outside of the pathline with a small angle ϵ. By definition of ψ (Fig. 7), this orientation corresponds to $\psi = \pi/2 - \epsilon$. Then, since $\psi > 0$, the particle migrates outwards ($dr/dt > 0$) with a clockwise tumbling ($d\psi/dt < 0$). When ψ gets negative, then the head of the particle (note that the head and tail are exchanged at $\psi = 0$) is inside the pathline. Then, the particle is attracted towards the vortex ($dr/dt < 0$). However, ψ gets continuously smaller and tends to $\psi = -\pi/2$ corresponding to the orientation that the major axis of the particle is parallel to the pathline. Then, when the particle further rotates, then it returns to the initial orientation with $\psi = \pi/2 - \epsilon$; recall again that $\psi = +\pi/2$ and $-\pi/2$ are the same orientation. Thus, the described motion is consistent with the observed periodic motion (Fig. 6) for the rigid spheroidal particle. The model also explains the observed fact in Fig. 6 that more anisotropic particle can be attracted more rapidly because the larger degree T of anisotropy corresponds to larger $|W_-|$ and larger L. Note that, according to Eq. (28), $|dr/dt|$ is proportional both to $|W_-|$ and L.

Next, we discuss the behavior of the elastic particles examined in Sec. III. When Ca is large enough [see Fig. 1(a) for example], the elastic particle is deformed in an initial period ($t' \lesssim 5$) and T has finite values [Fig. 4(a)]. Note that larger T corresponds to the larger magnitude of W_-, which is negative in the Taylor–Green vortical flow. Therefore, (28) implies that the attraction ($dr/dt < 0$) towards the vortex occurs when $\psi < 0$. This is indeed the case as demonstrated in Fig. 8(a). Hence, the simple model equation (28) also explains the radial attraction of the elastic particles in the initial period. Furthermore, as the particle approaches the vortex center, the deformation is relaxed [Fig. 1(a)–1(iii)], which corresponds to the decline in T [Fig. 4(a)] and therefore W_- also gets smaller; as a result, $|dr/dt|$ decreases so that the particle can stay around the vortex center. In fact, Fig. 8(b) shows that the average $|\langle T \sin\psi\rangle_{0\leqslant t'\leqslant 2}|$, in an initial period, of the product of the degree

T of deformation and the sine of the angle ψ between the major axis and the radial direction is an increasing function of Ca. This is consistent with the results shown in Fig. 2(b) that softer (i.e., larger Ca) particles can be more rapidly attracted by vortex. Incidentally, if we decrease the length L of the rod with time, then the rod model, Eqs. (28) and (29), can numerically reproduce the behavior of the deformable particles in a qualitative manner. It is also worth mentioning that the model can explain the observation in Ref. [31] that the migration of deformable vesicle particles is determined by the angle of the particle with respect to the pathline in the Taylor–Green vortex flow.

Thus, by using the governing equations (28) and (29) for the rod model in vortical flow, we may explain the essence of the behavior of the anisotropic particles: namely, the rigid spheroidal particles and the deformable elastic particles. In summary, the degree of particle anisotropy and the angle ψ between the major axis of particle and the radial direction are the two important parameters for the attraction of neutrally buoyant particles towards a vortex.

V. CONCLUSION

We have investigated the motion of a single neutrally buoyant hyperelastic particle in Taylor–Green vortices (13) by means of DNS with the full Eulerian finite difference method [32]. The parameters controlling this system is $\widetilde{D}$ (the initial diameter of the particle normalized by the vortex size), Ca (the capillary number), Re_p (the particle Reynolds number), and ξ (the viscosity ratio). Fixing $\widetilde{D}$ $(= 0.375)$, Re_p $(= 0.01)$, and ξ $(= 1)$, we have investigated Ca-dependence in the range $0.1 \leqslant \mathrm{Ca} \leqslant 10$. Then, we have found an interesting event that softer particles can be attracted towards a vortex center [Figs. 1(a), 2, and 3]. We quantify the degree of the deformation by the Taylor parameter (17) to show that more deformed particle can be attracted to the vortex more rapidly [Figs. 2(b) and 4(b)].

We emphasize that the deformation is a necessary condition for neutrally buoyant particles to be attracted by vortex. In fact, an additional DNS of a rigid spheroidal particle demonstrate that it is periodically attracted and repulsed by vortex [Figs. 5 and 6(a)]. It is of importance that the orientation of the anisotropic particle determines the motion in the radial direction; more precisely, if the particle is inwardly inclined with respect to the pathline (i.e., the angle ψ, defined in Fig. 7, is negative), then the particle is attracted towards the vortex; otherwise, it is repulsed (Fig. 6). This behavior is also confirmed in the rod model [Fig. 7(b)] examined in Sec. IV B. The derived equation (28) implies that the sign of dr/dt is determined by that of ψ.

On the basis of these analyses, we may explain the physical mechanism of the attraction of the elastic particles towards a vortex center. The elastic particle is strongly deformed by shear flow around a vortex, and the particle is inclined inwards with respect to the pathline [i.e., $\psi < 0$; see Fig. 8(a)], it accumulates into the center of vortex. Then, the deformation is relaxed gradually as the particle approaches the vortex center [Fig. 4(a)] and therefore it cannot move in the radial direction to stay around the vortex center.

Some issues are left for future studies. First, in the present study, we have restricted ourselves in the case with a single-scale vortical flow. As discussed in the Introduction, however, it is more interesting to investigate the effect of deformability of particles on the particle clustering in turbulent flows. Since high-Reynolds-number turbulence is composed of a hierarchy of coherent tubular vortices [9–12], we may extend the present analysis for single-scale flow to turbulence by taking into account its multi-scale nature. Such an extended investigation may lead to a deeper understanding of the results [29,30,44] in more realistic situations. Another future study is about the effect of particle deformation on the cross-sectional migration (i.e., the axial concentration [45]) in a tube. In particular, when the tube is curved, it is important to understand the effects of cross-sectional secondary flow (the Dean vortex) [26]. The present system is much simpler than flow in a tube because there is neither wall nor shear flow in the axial direction. Nevertheless, the proposed action due to swirling flow may affect the phenomenon in a curved tube. Furthermore, since the main aim of the present article is to demonstrate the attraction of deformable particles towards a vortex, more systematic parameter survey is left for a future study. For example, it is interesting to investigate other cases with different values of ξ and $\widetilde{D}$. The latter is particularly interesting because Eq. (28) implies that the speed of the radial migration is proportional to particle size. It is also important to study competition between the present effect due to particle deformation and the inertial effects (i.e., finite τ_p effects due to a mass density difference in particle and fluid) on particle clustering in vortical flow.

ACKNOWLEDGMENTS

This study was partly supported by JSPS Grants-in-Aid for Scientific Research (No. 20H02068, No. 21K20403, and No. 23K13253). The DNS were conducted under the supports of the NIFS Collaboration Research Program (No. 22KISS010) and by using the supercomputer Fugaku provided by RIKEN through the HPCI System Research Projects (No. hp210207 and No. hp220232). We also thank the anonymous referee who let us know the relevant recent study [31].

APPENDIX: DNS OF RIGID PROLATE SPHEROIDAL PARTICLES

In this Appendix, we describe the numerical methods and parameters for the DNS, which is used in Sec. IV A, of a rigid prolate spheroidal particles in the Taylor–Green vortical flow.

1. Numerical method

Fluid is governed by the continuity equation with $\alpha = f$ in Eq. (3) and the Navier–Stokes equation,

$$\frac{\partial v_i^{(f)}}{\partial t} + v_j \frac{\partial v_i^{(f)}}{\partial x_j} = -\frac{1}{\rho}\frac{\partial p}{\partial x_i} + \frac{\mu^{(f)}}{\rho}\frac{\partial^2 v_i^{(f)}}{\partial x_j^2} + f_i + f_i^{\leftarrow p}, \tag{A1}$$

where $f_i^{\leftarrow p}$ is the force due to particles. We employ an immersed boundary method originally proposed by Uhlmann [33] and improved by Kempe and Fröhlich [34] to simulate neutrally buoyant rigid particles. In this method, the fluid-particle interface is represented by a set of Lagrangian points distributed uniformly on it. To obtain uniform distribution of the points, we first locate points spirally on the surface of the spheroid [46]; and then we simulate point charges, with this distribution as the initial condition, moving on the spheroidal surface to obtain an uniform state with the minimum potential energy [47]. We evaluate the fluid-particle interaction force so that the nonslip boundary condition of fluid velocity is satisfied on each Lagrangian point. By interpolating the adjacent forces, we obtain the force $f_i^{\leftarrow p}$ in Eq. (A1) acting on the Eulerian grid. For the spatial discretization of the other terms in Eq. (A1), we use a second-order central difference scheme on the staggered grid. We temporally integrate the convection and viscous terms by the second-order Crank–Nicolson and Adams–Bashforth methods, respectively.

As for particle motions, we evaluate the force $\boldsymbol{F}^{\leftarrow f}$ and the moment $\boldsymbol{L}^{\leftarrow f}$ around the particle center acting on the particle by integrating the reaction force $-\boldsymbol{f}^{\leftarrow p}$ on its surface. Then, we numerically integrate Newton's equations of motion,

$$m\frac{d\boldsymbol{v}}{dt} = \boldsymbol{F}^{\leftarrow f} \tag{A2}$$

and

$$\frac{d\boldsymbol{I\omega}}{dt} = \boldsymbol{L}^{\leftarrow f}, \tag{A3}$$

where m, $\boldsymbol{I}$, $\boldsymbol{v}$, and $\boldsymbol{\omega}$ are the mass, inertial moment, velocity, and angular velocity of the particle.

We solve Eqs. (A2) and (A3) in the frame attached to the particle with the origin being the particle mass center and with axes being the major and minor axes of the spheroidal particle. We express the transformation between the two frames by the quaternion. Numerically evolving the quaternion, we obtain the particle orientation. More details of the numerical method are found in Ref. [48].

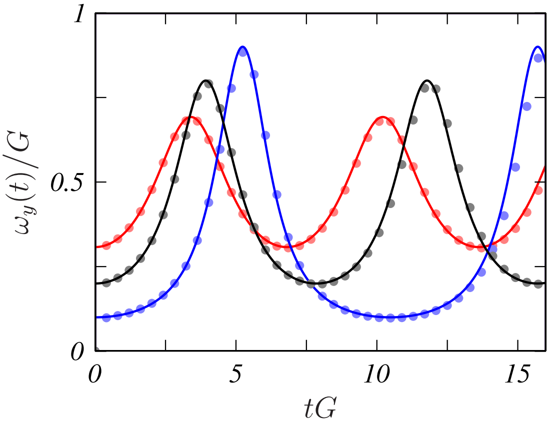

FIG. 9. Temporal evolution of the rotational speed for a rigid spheroidal particle in the Couette flow. Solid lines denote the analytical solutions by Jeffery [49], and circles are the result of the present DNS. Different colors correspond to different values of the Taylor parameter: red, $T = 1.5$; black, 2; blue, 3.

2. Numerical parameters

Similarly to the case for elastic particles, to investigate the behavior of a particle in a vortical flow, we impose the external force (14) that induces four vortices in a periodic cube. The global Reynolds number is set to be sufficiently small (Re = 0.1). We distribute a single spheroidal particle around one of these vortices whose major axis is initially parallel to the pathline. Fixing its sphere-converted diameter $D = 2(ab^2)^{1/3} = \pi/4$ (a and b are major and minor radii, respectively), we examine three cases for particles with different aspect ratios: $a/b = 1.5$, 2, and 3; i.e., $T = 0.2$, 0.33, and 0.5, respectively. We set the number of grid points of the DNS 256^3 so that particles are well resolved ($D/\Delta x = 32$).

3. Validations

Jeffrey [49] theoretically derived the temporal evolution of the rotational speed of a spheroidal particle without inertia in the Couette flow. Here, to validate the present DNS, we simulate three cases of a prolate spheroidal particle in the Couette flow with the shear rate $G = 0.004$ with three different values of the Taylor parameter ($T = 0.2$, 0.33, and 0.5). In each case, we set the major and minor radii of the spheroid as $(a, b) = (6,4)$, (8,4), and (12,4); therefore, the particle Reynolds number is small ($GD^2/\nu^{(f)} = 0.5$). The Couette flow is driven by two walls moving in opposite directions. The numbers of the grid points are 128 in the wall-normal direction and 256 in the other directions. The grid widths are uniform, and therefore particles in each case are resolved with $D/\Delta x = 18.3$, 20.2, and 23.1. Looking at the temporal evolution for the rotational speed, ω_y, shown in Fig. 9, we verify that the DNS results are in almost perfect agreement with the theoretical curves in all the three cases with $T = 1.5$, 2, and 3.

---

[1] K. D. Squires and J. K. Eaton, Preferential concentration of particles by turbulence, Phys. Fluids **3**, 1169 (1991).

[2] K. D. Squires and J. K. Eaton, Particle response and turbulence modification in isotropic turbulence, Phys. Fluids **2**, 1191 (1990).

[3] J. Bec, L. Biferale, M. Cencini, A. Lanotte, S. Musacchio, and F. Toschi, Heavy particle concentration in turbulence at dissipative and inertial scales, Phys. Rev. Lett. **98**, 084502 (2007).

[4] H. Yoshimoto and S. Goto, Self-similar clustering of inertial particles in homogeneous turbulence, J. Fluid Mech. **577**, 275 (2007).

[5] S. Goto and J. C. Vassilicos, Sweep-stick mechanism of heavy particle clustering in fluid turbulence, Phys. Rev. Lett. **100**, 054503 (2008).

[6] A. D. Bragg, P. J. Ireland, and L. R. Collins, Mechanisms for the clustering of inertial particles in the inertial range of isotropic turbulence, Phys. Rev. E **92**, 023029 (2015).

[7] S. Oka, D. Watanabe, and S. Goto, Large-scale clustering of light small particles in developed turbulence, Phys. Fluids **33**, 031707 (2021).

[8] S. Oka and S. Goto, Generalized sweep-stick mechanism of inertial-particle clustering in turbulence, Phys. Rev. Fluids **6**, 044605 (2021).

[9] S. Goto, A physical mechanism of the energy cascade in homogeneous isotropic turbulence, J. Fluid Mech. **605**, 355 (2008).

[10] S. Goto, Y. Saito, and G. Kawahara, Hierarchy of antiparallel vortex tubes in spatially periodic turbulence at high Reynolds numbers, Phys. Rev. Fluids **2**, 064603 (2017).

[11] Y. Motoori and S. Goto, Generation mechanism of a hierarchy of vortices in a turbulent boundary layer, J. Fluid Mech. **865**, 1085 (2019).

[12] Y. Motoori and S. Goto, Hierarchy of coherent structures and real-space energy transfer in turbulent channel flow, J. Fluid Mech. **911**, A27 (2021).

[13] C. Marchioli and A. Soldati, Mechanisms for particle transfer and segregation in a turbulent boundary layer, J. Fluid Mech. **468**, 283 (2002).

[14] C. Marchioli, A. Giusti, M. V. Salvetti, and A. Soldati, Direct numerical simulation of particle wall transfer and deposition in upward turbulent pipe flow, Int. J. Multiphase Flow **29**, 1017 (2003).

[15] F. Picano, G. Sardina, and C. M. Casciola, Spatial development of particle-laden turbulent pipe flow, Phys. Fluids **21**, 093305 (2009).

[16] A. Soldati and C. Marchioli, Physics and modelling of turbulent particle deposition and entrainment: Review of a systematic study, Int. J. Multiphase Flow **35**, 827 (2009).

[17] L. Brandt, and F. Coletti, Particle-laden turbulence: Progress and perspectives, Annu. Rev. Fluid Mech. 2022 **54**, 159 (2022).

[18] Y. Jie, Z. Cui, C. Xu, and L. Zhao, On the existence and formation of multi-scale particle streaks in turbulent channel flows, J. Fluid Mech. **935**, A18 (2022).

[19] Y. Motoori, C.-K. Wong, and S. Goto, Role of the hierarchy of coherent structures in the transport of heavy small particles in turbulent channel flow, J. Fluid Mech. **942**, A3 (2022).

[20] Y. Motoori and S. Goto, Multiscale clustering of heavy and light small particles in turbulent channel flow at high Reynolds numbers, Int. J. Heat Fluid Flow **102**, 109166 (2023).

[21] J. N. Cuzzi, R. C. Hogan, J. M. Paque, and A. R. Dobrovolskis, Size-selective concentration of chondrules and other small particles in protoplanetary nebula turbulence, Astrophys. J. **546**, 496 (2001).

[22] R. A. Shaw, Particle-turbulence interactions in atmospheric clouds, Annu. Rev. Fluid Mech. **35**, 183 (2003).

[23] R. S. Cherry and E. T. Papoutsakis, Physical mechanisms of cell damage in microcarrier cell culture bioreactors, Biotech. Bioeng. **32**, 1001 (1988).

[24] L. P. Wang and M. R. Maxey, Settling velocity and concentration distribution of heavy-particles in homogeneous isotropic turbulence, J. Fluid Mech. **256**, 27 (1993).

[25] G. Segre and A. Silberberg, Radial particle displacements in poiseuille flow of suspensions, Nature (London) **189**, 209 (1961).

[26] S. Ebrahimi and P. Bagchi, Inertial and noninertial focusing of a deformable capsule in a curved microchannel, J. Fluid Mech. **929**, A30 (2021).

[27] M. Maxey, The gravitational settling of aerosol particles in homogeneous turbulence and random flow field, J. Fluid Mech. **174**, 441 (1987).

[28] S. S. Ray and D. Vincenzi, Droplets in isotropic turbulence: Deformation and breakup statistics, J. Fluid Mech. **852**, 313 (2018).

[29] A. Hajisharifi, C. Marchioli, and A. Soldati, Particle capture by drops in turbulent flow, Phys. Rev. Fluids **6**, 024303 (2021).

[30] A. Hajisharifi, C. Marchioli, and A. Soldati, Interface topology and evolution of particle patterns on deformable drops in turbulence, J. Fluid Mech. **933**, A41 (2022).

[31] G. Kabacaoğlu and E. Lushi, Cross-stream migration of a vesicle in vortical flows, Phys. Rev. E **107**, 044608 (2023).

[32] K. Sugiyama, S. Ii, S. Takeuchi, S. Takagi, and Y. Matsumoto, A full eulerian finite difference approach for solving fluid–structure coupling problems, J. Comput. Phys. **230**, 596 (2011).

[33] M. Uhlmann, An immersed boundary method with direct forcing for the simulation of particulate flows, J. Comput. Phys. **209**, 448 (2005).

[34] T. Kempe and J. Fröhlich, An improved immersed boundary method with direct forcing for the simulation of particle laden flows, J. Comput. Phys. **231**, 3663 (2012).

[35] T. Gültop, On the propagation of acceleration waves in incompressible hyperelastic solids, J. Sound Vib. **264**, 377 (2003).

[36] A. J. Gil, Structural analysis of prestressed saint Venant–Kirchhoff hyperelastic membranes subjected to moderate strains, Comput. Struct. **84**, 1012 (2006).

[37] S. Takeuchi, Y. Yuki, A. Ueyama, and T. Kajishima, A conservative momentum-exchange algorithm for interaction problem between fluid and deformable particles, Int. J. Numer. Methods Fluids **64**, 1084 (2010).

[38] F. H. Harlow and J. E. Welch, Numerical calculation of time-dependent viscous incompressible flow of fluid with free surface, Phys. Fluids **8**, 2182 (1965).

[39] A. Albadawi, D. B. Donoghue, A. J. Robinson, D. B. Murray, and Y. M. C Delauré, Influence of surface tension implementation in volume of fluid and coupled volume of fluid with level set methods for bubble growth and detachment, Int. J. Multiphase Flow **53**, 11 (2013).

[40] M. S. Dodd and A. Ferrante, A fast pressure-correction method for incompressible two-fluid flows, J. Comput. Phys. **273**, 416 (2014).

[41] R. Jayaram, Y. Jie, L. Zhao, and H. I. Andersson, Preferential orientation of tracer spheroids in evolving Taylor–Green vortex flow, Phys. Fluids **34**, 043310 (2022).

[42] D. Alghalibi, M. E. Rosti, and L. Brandt, Inertial migration of a deformable particle in pipe flow, Phys. Rev. Fluids **4**, 104201 (2019).

[43] See Supplemental Material at http://link.aps.org/supplemental/10.1103/PhysRevFluids.9.014301 for a movie of Fig. 1(a).

[44] M. P. A. Assen, C. S. Ng, J. B. Will, R. J. A. M. Stevens, D. Lohse, and R. Verzicco, Strong alignment of prolate ellipsoids in Taylor–Couette flow, J. Fluid Mech. **935**, A7 (2022).

[45] C. K. W. Tam and W. A. Hyman, Transverse motion of an elastic sphere in a shear field, J. Fluid Mech. **59**, 177 (1973).

[46] E. B. Saff and A. B. J. Kuijlaars, Distributing many points on a sphere, Math. Intell. **19**, 5 (1997).

[47] M. N. Ardekani, P. Costa, W. P. Breugem, and L. Brandt, Numerical study of the sedimentation of spheroidal particles, Int. J. Multiphase Flow **87**, 16 (2016).

[48] A. Eshghinejadfard, S. A. Hosseini, and D. Thévenin, Fully-resolved prolate spheroids in turbulent channel flows: A lattice Boltzmann study, AIP Adv. **7**, 095007 (2017).

[49] G. B. Jeffery, The motion of ellipsoidal particles immersed in a viscous fluid, Proc. R. Soc. London A **102**, 161 (1922).